A time-continuous land surface temperature (LST) data fusion approach based on deep learning with microwave remote sensing and high-density ground truth observations

Jiahao Han [a,b], Shibo Fang [b,*], Qianchuan Mi [a,b], Xinyu Wang [b], Yanru Yu [b], Wen Zhuo [b], Xiaofeng Peng [b]

[a] School of Atmospheric Sciences, Nanjing University of Information Science and Technology, Nanjing 210044, Jiangsu Province, China
[b] State Key Laboratory of Severe Weather, Chinese Academy of Meteorological Sciences, Beijing 100081, China

HIGHLIGHTS

- Time-continuous LST is monitored using deep learning.
- The high-density site and microwave data in "Earth big data" are used to monitor LST.
- Based on radiation transmission, a multi-source data fusion approach is proposed.
- The contribution of driving factors to LST is quantitatively assessed.

GRAPHICAL ABSTRACT
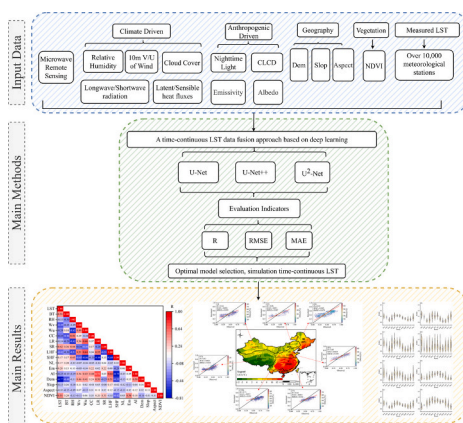
ARTICLE INFO

ABSTRACT

Land surface temperature (LST) is a crucial parameter in the circulation of water, exchange of land-atmosphere energy, and turbulence. Currently, most LST products rely heavily on thermal infrared remote sensing, which is susceptible to cloud and rain interference, leading to inferior temporal continuity. Microwave remote sensing has the advantage of being available "all-weather" due to strong penetration capability, which provides the possibility to simulate time-continuous LST data. In addition, the continuous increase in high-density station observations (>10,000 stations) provides reliable measured data for the remote sensing monitoring of LST in China. This study aims to adopt the "Earth big data" generated from high-density station observation and microwave remote sensing data to monitor LST based on deep learning (U-Net family) for the first time. Given the significant spatial and temporal variability of LST and its sensitivity to various factors according to radiation transmission equations, this study incorporated climatic, anthropogenic, geographical, and vegetation datasets to facilitate a multi-source data fusion approach for LST estimation. The results showed that the U-Net++ model with modified

* Corresponding author.
  E-mail address: fangshibo@cma.gov.cn (S. Fang).

skip connections better minimized the semantic discrepancy between the feature maps of the encoder and decoder subnetworks for 0.1° daily LST mapping across China than the U-Net and U²-Net deep learning models. The accuracy of the LST simulation exhibited favorable outcomes in the spatial and temporal dimensions. The station density met the requirements of monitoring air-ground integration monitoring in China. Additionally, the temporal change in the simulation accuracy fluctuated in a W-shape owing to the limited simulation capability of deep learning in extreme scenarios. Anthropogenic factors had the largest influence on LST changes in China, followed by climate, geography, and vegetation. This study highlighted the application of deep learning in remote sensing monitoring against the background of "big data" and provided a scientific foundation for the response of climate change to human activities, ecological environmental protection, and sustainable social and economic development.

1. Introduction

Land surface temperature (LST) is an essential parameter in climate, hydrology, ecology, biology, and agricultural production and serves as an excellent representation of water circulation, energy and turbulence exchange (Wang et al., 2014; Ermida et al., 2017; Zhang et al., 2021). LST affects the stability and balance between land-atmosphere circle and has been applied to study various subjects, such as urban heat islands (Nogueira et al., 2022), glacier melting (Davis et al., 2023), extreme drought (Anderson et al., 2011), forest fires (Westerling et al., 2006), volcanic earthquakes (Ouzounov and Freund, 2004), surface soil moisture (Ghahremanloo et al., 2018), climate change (Azarderakhsh et al., 2020), and related research (Li et al., 2023). In the context of climate warming, LST has been recognized as a high-priority parameter by the International Geosphere and Biosphere Program (Townshend et al., 1994) and an indispensable parameter in the land biosphere designated by the Global Climate Observing System (Hollmann et al., 2013). Therefore, a high-quality time-continuous LST dataset can provide an effective scientific basis for studies on agricultural production, ecological protection, disaster mitigation, and economic development.

With the development and improvement of satellite remote sensing, remote sensing has become the primary method for monitoring LST as it can estimate high-precision and long-duration LST data. There are two main types of remote sensing data: thermal infrared (TIR) and microwave. TIR estimations of LST have been extensively studied using MODIS, VIIRS, SLSTR, and SEVIRI satellites (Coll et al., 2012; Göttsche et al., 2016). However, TIR is greatly affected by clouds, rain, vegetation, and terrain, especially in hilly areas, and is thus more suitable for plains with clear skies, few clouds, and relatively homogeneous vegetation. LST monitoring using TIR has inferior temporal continuity owing to weather conditions and the underlying surface, with time scales of 8 or 16 d in general (Zhang et al., 2021). Microwave remote sensing data has the advantage of being available "all-weather" with negligible influence from cloudy, foggy, or other meteorological phenomena owing to the robust penetration capability, which can provide time-continuous observational data (Chen et al., 2022). However, passive microwave (PMW) inversion LST has a low spatial resolution (approximately 0.25°), such as that of the AMSR-E, SMM/I-SMMR, and AMSR-2 satellites (Royer and Poirier, 2010; Mao et al., 2018; Quan and Cheng, 2020). The monitoring accuracy of LST using microwaves has errors of approximately 1–10 k, which is worse than that using TIR of 0.2–2 k. This discrepancy is because microwave emissivity is more sensitive to spatial variation than TIR emissivity owing to the heterogeneous reflectivity and dielectric properties of soil moisture (Osińska-Skotak, 2007; Quan and Cheng, 2020). The application of microwave remote sensing inversion LST should be strengthened because it can provide time-continuous LST monitoring unaffected by complex terrain (Kohn and Royer, 2010; Marchand et al., 2018), which is useful for areas with complex terrain and variable climates, such as China.

The main methods for LST inversion using remote sensing include physical models and machine learning. Physical models mainly consist of single-channel, split-window/dual-window, temperature and emissivity separation, and physics-based day/night algorithms (Wan and Li, 1997; Malakar and Hulley, 2016). Although physical models can describe LST inversion mechanisms based on environmental variables and remote sensing, they depend on knowledge and understanding of the model parameters. Due to uncertainties owing to the complexity of physical processes and variations between periods and regions, physical models tend to have limited accuracy in complex environmental remote sensing (Yuan et al., 2020). Therefore, machine learning (ML) plays an important role in monitoring LST to produce continuous spatiotemporal LST data. Deep learning (DL), a typical cutting-edge ML framework, outperforms traditional models and is economical (Lee et al., 2018; Reichstein et al., 2019). Compared to traditional ML models, DL can extract multiscale and multilevel features from remote sensing by fusing these features, which allows for a highly accurate inversion of LST (LeCun et al., 2015; Zhang et al., 2016). A substantial number of DL frameworks, such as neural networks, artificial neural networks, multilayer perceptron, and convolutional neural networks, have been applied to simulate LST with good accuracy (Mao et al., 2008; Wang et al., 2013; Mao et al., 2018; Penghai et al., 2019; Tan et al., 2019). The U-Net family is a classical approach to framework design with extensive applications in image segmentation and recognition, including U-Net, U-Net++, and U²-Net (Ronneberger and Brox, 2015; Zhou et al., 2018; Qin et al., 2020). This architectural structure is founded on several interconnected convolutional layers that assess data at various levels of aggregation, leading to multiscale feature coding of images, automatic recognition of regions of interest, and delivery of consistent technical support for the monitoring of surface information in intricate backgrounds (Wu et al., 2021; Lobert et al., 2023). Furthermore, the U-Net family has several benefits, including a straightforward architecture, reduced requirements for model training and inference, and rapid computation time, all of which make it a popular choice for environmental remote-sensing monitoring applications (Wang et al., 2021; Chen et al., 2023; Dalagnol et al., 2023).

Highly precise and reliable labeled data are essential for DL simulation accuracy. The China Meteorological Administration can provide high-density LST observation station data for all of China (>10,000 stations), which can improve the accuracy of the simulated and evaluated models in different DL frameworks. However, the density of observation stations in different regions is not the same, which is limited by the economic level and natural environment. Relevant studies have not been conducted on the effect of station density on LST simulation accuracy. According to the physical equations of radiation transmission, the spatiotemporal variation in LST is affected by various factors, including climatic and anthropogenic factors, geography, and vegetation (Li et al., 2013; Karimi Firozjaei et al., 2022). In the background of "Earth big data," the fusion and utilization of multiple data is crucial to improve the accuracy of LST monitoring. Overall, incorporating the equilibrium radiation equations and inputting the factors that influence LST into the DL model can not only combine the physical mechanism and the DL model to enhance the simulation accuracy but also separate the contribution of each feature to LST. To date, the contributions of each factor to the predictor variables have not been elucidated due to the limitations of the DL algorithm.

This study aims to utilize "Earth big data" generated from high-density station observations and microwave remote sensing data to monitor LST using DL model for the first time. The study incorporates

climate, anthropogenic, geographical, and vegetation datasets to facilitate a multi-source data-fusion approach for LST estimation based on radiation transmission equations. Furthermore, the contributions of climate-driven, anthropogenic, geographical, and vegetation variables to LST were analyzed. This study facilitates the integration of satellite and high-density ground-truth observation data sources to uncover the underlying knowledge and principles present in "Earth big data", thereby qualitatively improving the accuracy and utility of Earth's big data.

2. Study area and data

2.1. Study area

China is located in eastern Asia on the west coast of the Pacific Ocean, with a total territorial area of about 9.6 million km² (Tan et al., 2019). China can be divided into seven natural regions according to climate, geographical location, and topography (Fig. 1): (I) the warm-temperate desert of northwest China, (II) the temperate grassland of Inner Mongolia, (III) the temperate humid and sub-humid northeast China, (IV) the warm-temperate humid and sub-humid north China, (V) the subtropical humid central and south China, (VI) the Qinghai-Tibetan Plateau, and (VII) the tropic humid south China (Yao et al., 2018). >10,000 daily LST meteorological observation stations (including removal and exchange) were provided from 2015 to 2021 by the China Meteorological Administration (http://idata.cma/cmadaas). The density of stations in each natural region was calculated by comparing the number of stations to the total area in the following descending order: IV > V > VII > III > II > I > VI.

2.2. Data

2.2.1. FY-3 satellite products

The microwave imager (MWRI) equipped on the FY-3 satellite possesses five frequencies, each with two polarization modes, enabling it to furnish precise information pertaining to various parameters such as LST, soil moisture, floods and droughts, snow depth, typhoon structure, and atmospheric water content, etc. (Wang et al., 2022; Zhou et al., 2023) This study used FY-3C (2015–2019) and FY-3D (2020−2021) microwave bright temperature (BT) data with 10 km spatial resolution (http://data.nsmc.org.cn/). A past study showed that the R² of different

microwave remote sensing methods in the FY-3 satellite data exceeds 0.98, signifying a commendable concordance (Wang et al., 2022).

2.2.2. Climate driven

According to the equilibrium radiation equation, LST alteration is primarily driven by long- and short-wave radiation (Wild, 2015). LST is directly influenced by latent heat and sensible heat fluxes (Li et al., 2013; Donohoe et al., 2014). Additionally, relative humidity and wind speed (10 m U/V) can cause turbulence on the surface, affect energy exchange, and subsequently modify LST (Compo and Sardeshmukh, 2009). Cloud cover can alter the intake of shortwave radiation as well as the emission of surface inverse radiation, ultimately leading to changes in LST (Stephens and Webster, 1981). Hourly data were collected from the fifth-generation European Center for Medium-Range Weather Forecasts atmospheric reanalysis of the global climate (ERA5-Land) with a 0.1° spatial grid cell resolution (https://cds.climate.copernicus.eu).

2.2.3. Anthropogenic driven

Land constitutes a fundamental medium for human activities and the change in its utilization type is a direct manifestation of the process and results of human influence on the land surface. This influence can bring about direct alterations in surface albedo and emissivity, rendering land cover one of the most significant determinants of LST (Kafy et al., 2020). The utilization of night-light data provides insight into the low light intensity emanating from urban lights and traffic and facilitates the differentiation of human activities across various types of land use, which further enables the identification of changes in population density and aerosol concentration (Pfeifroth et al., 2018; Liu et al., 2022). The yearly land cover with 30 m spatial resolution was provided by China Land Cover Dataset (CLCD) from the Geospatial Data Institute (Yang and Huang, 2021), hourly albedo data with 0.1° resolution was provided by ERA5-Land, 16-days emissivity with 1 km spatial resolution was provided by MODIS (MOD11A2) (https://lpdaac.usgs.gov), monthly night-light with 500 m spatial resolution was collected from VIIRS (https://www.earthdata.nasa.gov).

2.2.4. Geography

The geographical factors of altitude, slope, and aspect significantly impact the radiation balance of the land surface at varying elevations and orientations, ultimately influencing LST (Phan et al., 2018). The Geospatial Data Cloud provided the derivation of geographical
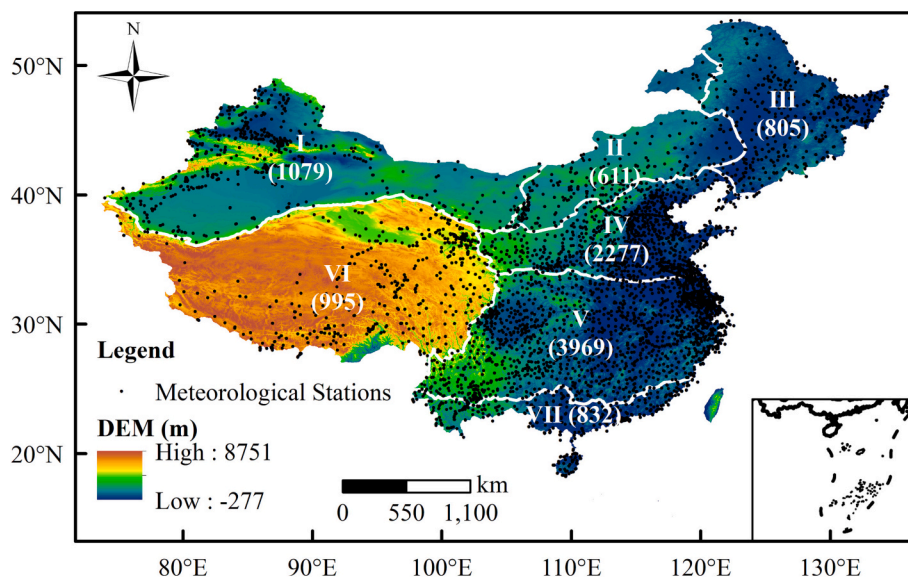

Fig. 1. Geological information, DEM, meteorological stations distribution, and natural region divisions in China (Roman numerals: natural region divisions; Arabic numerals: the number of meteorological stations in the natural region).

information with a 90 m spatial resolution (https://www.gscloud.cn).

2.2.5. Vegetation

Vegetation primarily influences LST through energy and water exchange in the atmosphere, encompassing two key domains: physical and chemical processes (Thakur et al., 2022). Physical processes pertain to the modification of the LST through alterations in surface albedo, ground roughness, and cooling of the adjacent environment through evapotranspiration (Peñuelas et al., 2009; Abera et al., 2020). Biochemical processes refer to the mechanisms through which alterations in vegetation impact long-(short-) wavelength radiation by regulating changes in atmospheric aerosols and greenhouse gases, leading to subsequent modifications in LST (Donohoe et al., 2014; Wild, 2015). For this study, 16-d NDVI (Normalized Difference Vegetation Index) data with a 250 m spatial resolution were provided by MODIS (MOD13A2) (https://lpdaac.usgs.gov).

In total, daily LST observations with climate-driven, anthropogenic, geographical, and vegetation data were collected (Table 1). All data were subjected to quality control measures and were interpolated to a grid size of 0.1° using the bilinear interpolation method for consistency, then the data underwent rotation and enhancement procedures. The FY-3 satellite operates in a polar orbit, with the FY-3C satellite passing over the local equator at 10:15 for its descending local time and 22:15 for its ascending local time. Meanwhile, the FY-3D satellite has a local equatorial crossing time of 02:00 for descending and 14:00 for ascending (Wang et al., 2022). First, the transit time of FY-3 satellite and hourly ERA5-Land were recorded in Universal Time Coordinated (UTC), while the actual measured LST was in Beijing time and was then converted to UTC. Then, the transit time of FY-3 satellite was rounded to the nearest hour in order to be matched with the hourly auxiliary data. Non-hourly auxiliary data, such as NDVI, NL, Em, CLCD, and geographical information, exhibited relatively stable state over a period of time. Therefore, non-hourly auxiliary data from the corresponding time period was utilized to match the all transit time of satellite data. The combination of satellite and hourly auxiliary data yielded high-frequency information,

while non-hourly auxiliary data contributed low-frequency information about the background field. The adaptive learning of DL model enabled it to dynamically obtain daily average LST for each satellite transit area. Finally, a total of 17,766 time-matched samples with remote sensing and auxiliary data values were identified to form the experimental datasets. It is important to recognize that the NL value is highly differentiated in space, which can potentially result in suboptimal outcomes. To mitigate these variations, an exponential transformation was applied to the initial values.

3. Methodology

The research flowchart is shown in Fig. 2 including the input data, DL structure, evaluation indicators, and relative importance (RI) of each factor for LST. The FY-3 microwave BT and auxiliary data were employed as input features in the DL network framework. The evaluation indicators were used to validate the precision of the simulated and measured LST. Climate-driven, anthropogenic, geographical, and vegetation factors were excluded from the trained DL framework to explore the contribution of each factor to LST using the RI formula.

3.1. U-Net family DL framework

The U-Net family of DL models represents a semantic segmentation framework with a multitude of applications in image segmentation, primarily encompassing U-Net, U-Net++, and U²-Net. The U-Net architecture exhibits completely symmetrical traits and incorporates skip connections, thereby conferring the benefits of minimal input parameters and superior learning precision (Ronneberger and Brox, 2015). The U-Net++ architecture incorporates nested and dense jump connections, with reconfigured skip pathways specifically intended to mitigate the semantic gap between the feature maps of the encoder and decoder subnetworks (Zhou et al., 2018). The U²-Net architecture is a two-level nested U-structure that effectively captures a large amount of contextual information across various scales owing to the amalgamation of receptive fields of varying sizes of proposed Residual U-blocks (RSUs) (Qin et al., 2020). The U-Net family comprises four components: image input, encoding, decoding, and image output. In the present study, the resampled FY-3 microwave BT and auxiliary data (climate-driven, anthropogenic, geography, and vegetation) were incorporated into the DL framework. In DL model, the input batch size, number of iterations, loss function (Weights-MSE loss and MSE loss functions), and optimizer (Adam and SDG) were crucial parameters that required repeated adjustments.

3.2. Evaluation indicators

To verify whether the model was temporally predictable, we established 2015–2019 (12,892 matched samples) as the training period, 2020 (2331 matched samples) as the validation period, and 2021 (2543 matched samples) as the testing period. A comparison between the simulated and observed LST was conducted to assess the accuracy of the model training process and determine the most suitable architecture and parameters. The evaluation indicators were calculated as follows:

$$RMSE = \sqrt{\frac{\sum_i (y_i - \widehat{y}_i)^2}{n}} \qquad (1)$$

$$MAE = \frac{\sum_i |y_i - \widehat{y}_i|}{n} \qquad (2)$$

$$R = \frac{\sum_{i=1}^{n} (y_i - \overline{y}_i)(\widehat{y}_i - \overline{\widehat{y}}_i)}{\sqrt{\sum_{i=1}^{n} (y_i - \overline{y}_i)^2} \sqrt{\sum_{i=1}^{n} (\widehat{y}_i - \overline{\widehat{y}}_i)^2}} \qquad (3)$$

Table 1
Abbreviation and spatial and temporal resolutions of the data used in this study.

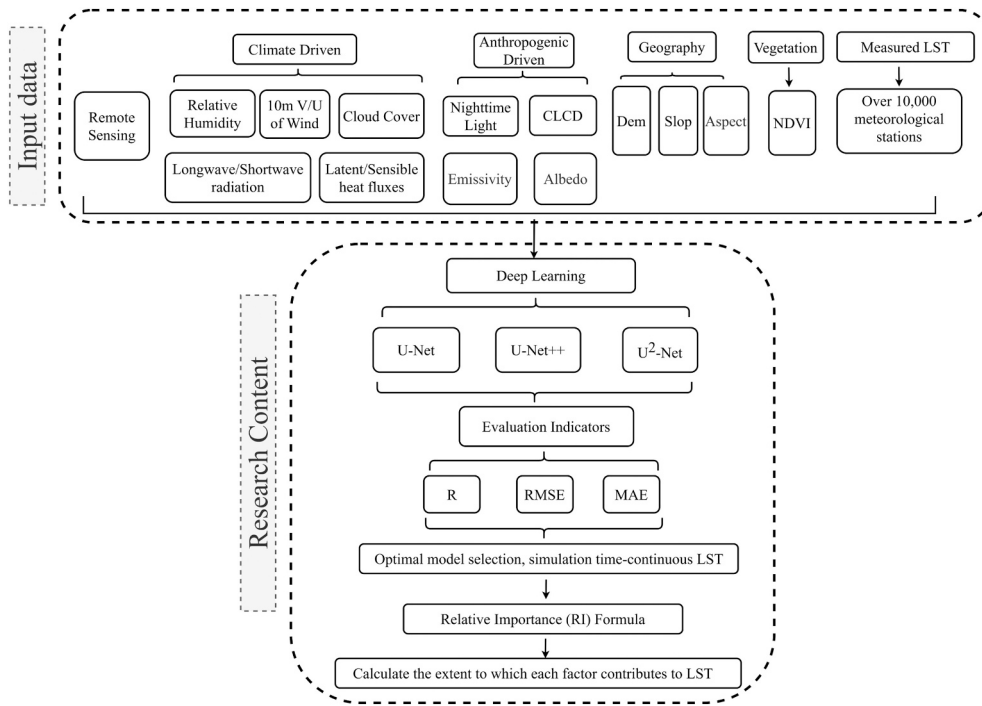| Classification	Abbreviation	Data	Spatial resolution	Temporal resolution
Remote sensing	BT	FY-3C/3D MWRI bright temperature	10 km	Daily
Measured	LST	Land surface temperature	Stations	Daily
Climate driven	RH	Relative humidity	0.1°	Hourly
	Wv	10 m V of wind	0.1°	Hourly
	Wu	10 m U of wind	0.1°	Hourly
	CC	Cloud cover	0.1°	Hourly
	LR	Longwave radiation	0.1°	Hourly
	SR	Shortwave radiation	0.1°	Hourly
	LHF	Latent heat fluxes	0.1°	Hourly
	SHF	Sensible heat fluxes	0.1°	Hourly
Anthropogenic driven	NL	Nighttime light	500 m	Monthly
	CLCD	China Land Cover Dataset	10 m	Yearly
	Em	Emissivity	1 km	16 d
	Al	Albedo	0.1°	Hourly
Geographical	Dem	–	90 m	–
	Slop	–	90 m	–
	Aspect	–	90 m	–
Vegetation	NDVI	Normalized difference vegetation index	250 m	16 d

Fig. 2. Research flowchart.

$$Loss_{(MSE)} = \frac{1}{n} \sum_{i=1}^{n} (y_i - \widehat{y}_i)^2 \tag{4}$$

$$Loss_{(Weights-MSE)} = \frac{1}{n} \sum_{i=1}^{n} |y_i - \widehat{y}_i| e^{|y_i - \widehat{y}_i|} \tag{5}$$

where y_i is the measured LST, $\widehat{y}_i$ is the simulated LST, and n is the total number of samples. The simulation is considered superior when the RMSE, MAE, and loss function are smaller and R is closer to 1.

3.3. Contribution calculations

A novel technique was proposed for the contribution calculations of convolutional neural network and recurrent neural network models. However, this approach was confined to models relying on vector datasets and is inapplicable to models incorporating 2D images or hybrid datasets (Wolanin et al., 2020). This study employed a frequently utilized approach to determine the RI of the DL model. This technique involves the stepwise removal of input features and calculation of the RI of features through the degree of variation in error (Song et al., 2016; Arigbe et al., 2018; Jeong et al., 2021). RI was calculated as follows:

$$Relative\ Importance\ (RI) = \frac{MSE_i}{\sum_{i=1}^{n} (MSE_{Reference} - MSE_i)} * 100\% \tag{6}$$

where MSE_i is the error of a variable after removal, $MSE_{Reference}$ is the error of the DL model training for all the input features, and n is the total number of input features. A larger error indicates that the model is more dependent on this feature.

4. Results

4.1. Descriptive statistics

Pearson correlation coefficients were calculated to evaluate the strong linear or non-linear relationships between the predictor variables and daily LST observations. Fig. 3 displays the calculated R values for all variables (remote sensing, climate-driven, anthropogenic, geographical, and vegetation), except for CLCD, which denotes categorical attributes rather than specific numerical quantities. The correlation coefficient between LST and remote sensing data (BT) was 0.51 and that between LST and climate-driven LST was 0.30. For the anthropogenically-driven factors, the average correlation coefficient was 0.23. For geographical factors, the DEM was strongly correlated with LST (R < -0.7). NDVI had a relatively moderate correlation with LST, with an R value of −0.51. Although there was a high correlation among various input factors, such as LR and Al, the physical mechanisms represented by each factor differ. LR is the amount of thermal radiation emitted by the atmosphere and clouds reaching the Earth's surface, whereas Al is a measure of the reflectivity of the Earth's surface. Despite the substantial impact of Al on LR, Al represents the underlying surface itself, while LR is intricately influenced by additional factors such as cloud cover, all of which significantly influence LST.

4.2. Model calibration and validation

In the study, the data comprising remote sensing, climate, anthropogenic, geography, and vegetation with 0.1° grid cell were input into the DL model to acquire LST at a satellite transit time and then fused into a daily LST. Notably, the Adam, SDG optimizer, Weights-MSE Loss, and MSE Loss functions were ultimately chosen for comparative analysis in the U-Net family (Table S1). Different DL model architectures, optimizers, and loss functions affect the accuracy of LST simulations. U-Net++ with the Adam optimizer and MSE loss function had the best accuracy of LST simulation compared to other combinations regardless of the training, validation, and test sets. The optimization of the model can be significantly affected by the magnitude of the batch size and number of iterations, thereby affecting the efficiency and efficacy of training the model. To ensure optimal simulation accuracy, a batch size of 16 was adopted for U-Net++ with the Adam optimizer and MSE Loss model (Table S2). After conducting numerous experiments, the model achieved convergence in approximately 170 iterations without any further loss. To guarantee the accuracy of the simulation, the number of
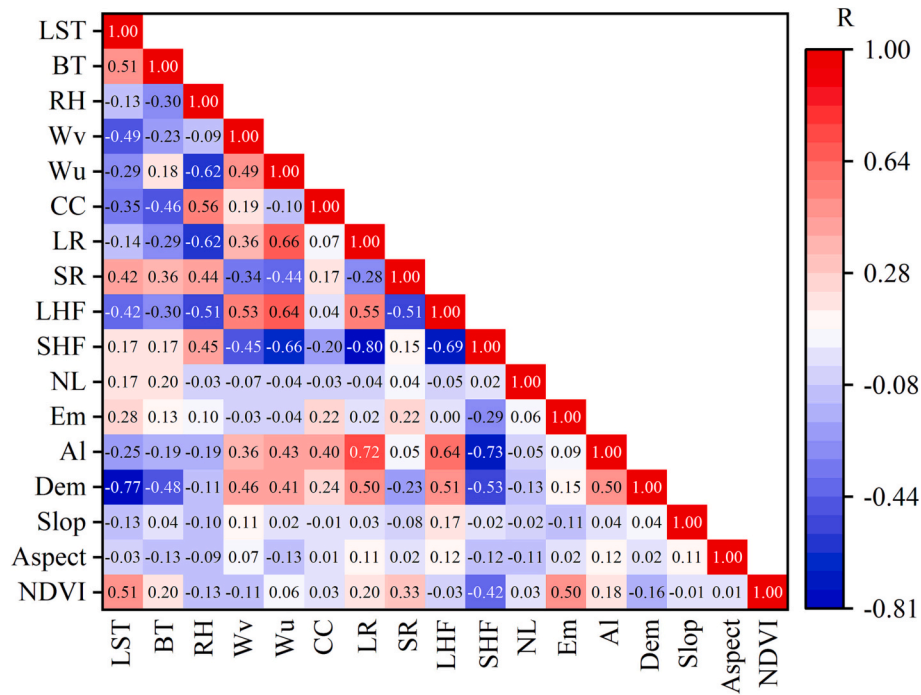
Fig. 3. Pearson correlation coefficient among the predictor variables and LST.

iterations was set to 200.

By applying all the above predictor variables in the U-Net++ framework, the daily LST across China was simulated and validated (Fig. 4). From comprehensive and quantitative perspective, the U-Net++ for LST of the training, validation, and test sets presented acceptable fits, with R ranging from 0.84 to 0.87, MAE from 0.049 to 0.056, and RMSE from 0.071 to 0.082. Although the simulated LST was slightly lower than the observed value, the simulation demonstrated a satisfactory overall outcome with applicability to the majority of China's regions.

4.3. Spatial evaluation of model performance

The model performance for the spatial patterns in different regions was calculated and the distribution of the test LST and point density plots of the observed and simulated LST in different regions are shown in Fig. 5. These results revealed that the spatial distribution of LST in China exhibited a declining trend from east to west. It can be observed from the point-density plots that different regions show good simulation results owing to the stability of the DL. In addition, the simulation results for region VII, which is located closer to the ocean, where the climate is often dominated by the sea surface temperature and monsoon, were relatively poor. This observation aligns with prior research outcomes as well (Benali et al., 2012). Moreover, the results for region V were superior compared to those for the other regions in this study, which is

attributable to the simpler topographic and environmental conditions. It is widely acknowledged that simulation accuracy is affected by station density (Shen et al., 2020); however, this study collected LST data from >10,000 stations and the results showed that the simulation accuracy was essentially the same at different station densities in different regions. This finding demonstrates that the current density of meteorological observation stations has met the needs of integrated airspace monitoring in China and that the layout of observation stations should focus on key areas and data quality in the future.

Previous studies revealed that the CLCD significantly influences LST (Li et al., 2013). By computing the RMSE based on the normalized LST, a comparative analysis was conducted to evaluate the model's performance across diverse land-cover types. Fig. S1a shows that wetland exhibits the best model performance. However, the RMSE for croplands, forests, shrubs, grasslands, water, and snow were more centralized. In addition to the above CLCD, the model performance for the DEM ranges is shown (Fig. S1b). LST has a significant relationship with the DEM, with LST generally decreasing as the DEM increases. There was no significant relationship between the simulation accuracy and DEM ranges, with the simulations being the worst at low altitudes (<1000 m) owing to complex land cover types. This non-significant observation may be attributed to ignoring high-density station data in previous investigations. The reduced number of observation stations at higher altitudes may have impeded the model accuracy, thereby emphasizing the importance of their inclusion in future studies.
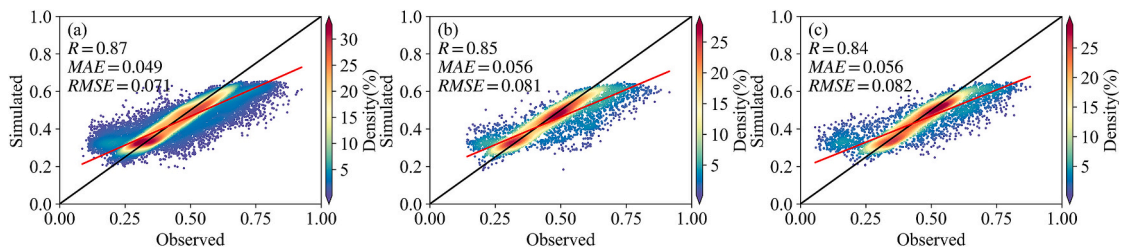

Fig. 4. Point density plots of observed and simulated normalized LST for the U-Net++ model: (a) training, (b) validation, (c): test
Note: The red line is the linear regression of the scattered dots, and the black line is the 1:1 line used as a reference.
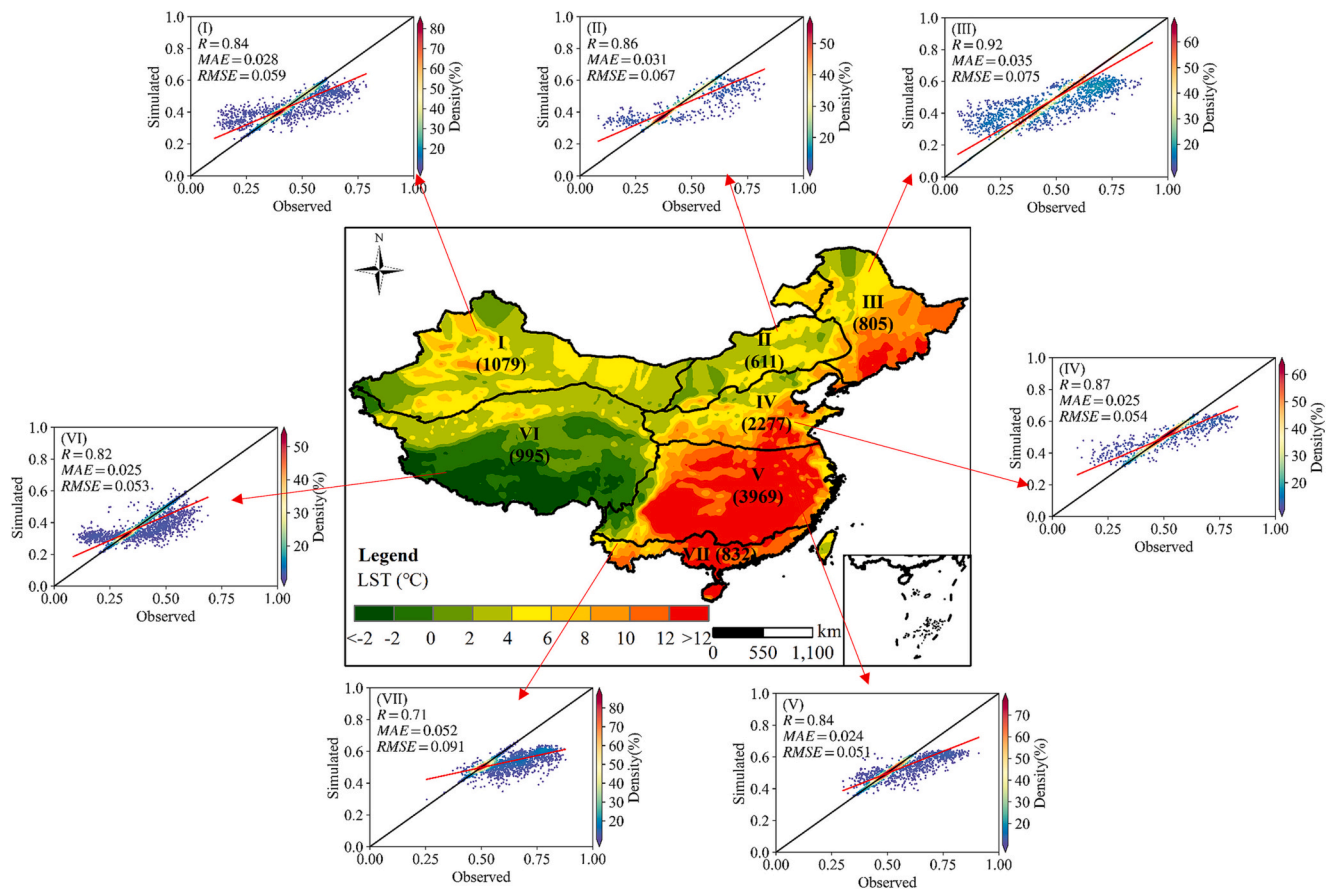
Fig. 5. Spatial distribution of test LST and point density plots of the observed and simulated normalized LST in different regions.

4.4. Temporal evaluation of model performance

For temporal analysis, the model performance at a monthly scale in different regions was evaluated. Fig. 6 shows violin plots of the RMSE distribution for each month in different regions. The average RMSE in China fluctuated with a W-shape pattern (Fig. 6a). At both extremely low and high temperatures (observed in January, May, and December), the RMSE attained its highest value, indicating poor model performance. The optimal simulation effect occurred when LST was close to the regional average. In addition, the RMSE for each month was concentrated near the average, demonstrating that the simulation findings remained unaffected by extreme values. For different regions (Fig. 6b–h), the average RMSE trend in regions I, II, III, IV, and VI was consistent with that of China overall, showing W-shapes. The average alteration in the RMSE exhibited an initial increase followed by a decline within regions V and VII. This phenomenon was attributed to the governing impact of the oceanic climate over the two regions, inducing a higher than average LST, ultimately culminating in suboptimal simulation outcomes. Notably, the RMSE box exhibited the most prominent amplitude in region III for almost all months but the average RMSE was not large. The significant influence of abrupt and intense cold episodes on the volatility of the regional RMSE can be attributed to the prevailing low temperatures and intricate terrain of the area. The findings revealed that the DL model exhibited limited simulation capability for extreme scenarios and the behavior was affected by diverse variables and was not solely reliant on remote sensing data. The findings generally emphasize the importance of incorporating temporal aspects into models to estimate LST.

4.5. Contributions of climate-driven, anthropogenic, geography, and vegetation for LST

The input features, including climate-driven, anthropogenic, geographical, and vegetative features, were used in Eq. (6) to analyze the RI of LST (Fig. 7). As shown in Fig. 7a, anthropogenic driving was the dominant factor affecting LST in China, with an RI of 40.05 %. The RIs for climate-driven, geography, and vegetation were 33.98 %, 31.87 %, and 30.72 %, respectively. The modification of the CLCD caused by anthropogenic activities directly impacted the transformation of surface matter and energy within inhabited regions. The underlying surface played a crucial role in the generation of climate, resulting in noteworthy consequences for the exchange of surface heat, momentum, water vapor, and interactions with the Earth's atmosphere. The release of heat generated by human activities along with intensified insulation of the atmosphere and inversion effects due to greenhouse gas emissions also had notable impacts. Meanwhile, the aforementioned effect has the potential to provoke direct transformations pertaining to surface albedo and emissivity, thereby positioning CLCD as one of the dominant factors contributing to the formation of LST. The monthly RI in China was calculated as shown in Fig. 7b. Overall, the influence of anthropogenic factors on LST was dominant in different months. In addition, the influence of anthropogenic driving is most pronounced in winter. The cause of this occurrence is not solely attributable to the reduction in vegetation and changes in the underlying surface and can be attributed to the combustion of fossil fuels in winter, which contributed to an increase in atmospheric aerosols and the consequent alteration of radiant flux. Simultaneously, the geographical component, serving as a comparatively constant contextual element, exerted a direct influence on LST via the associated static constraining factors of diminishing elevation, aspect, and mountain peak-to-valley depth, which affected
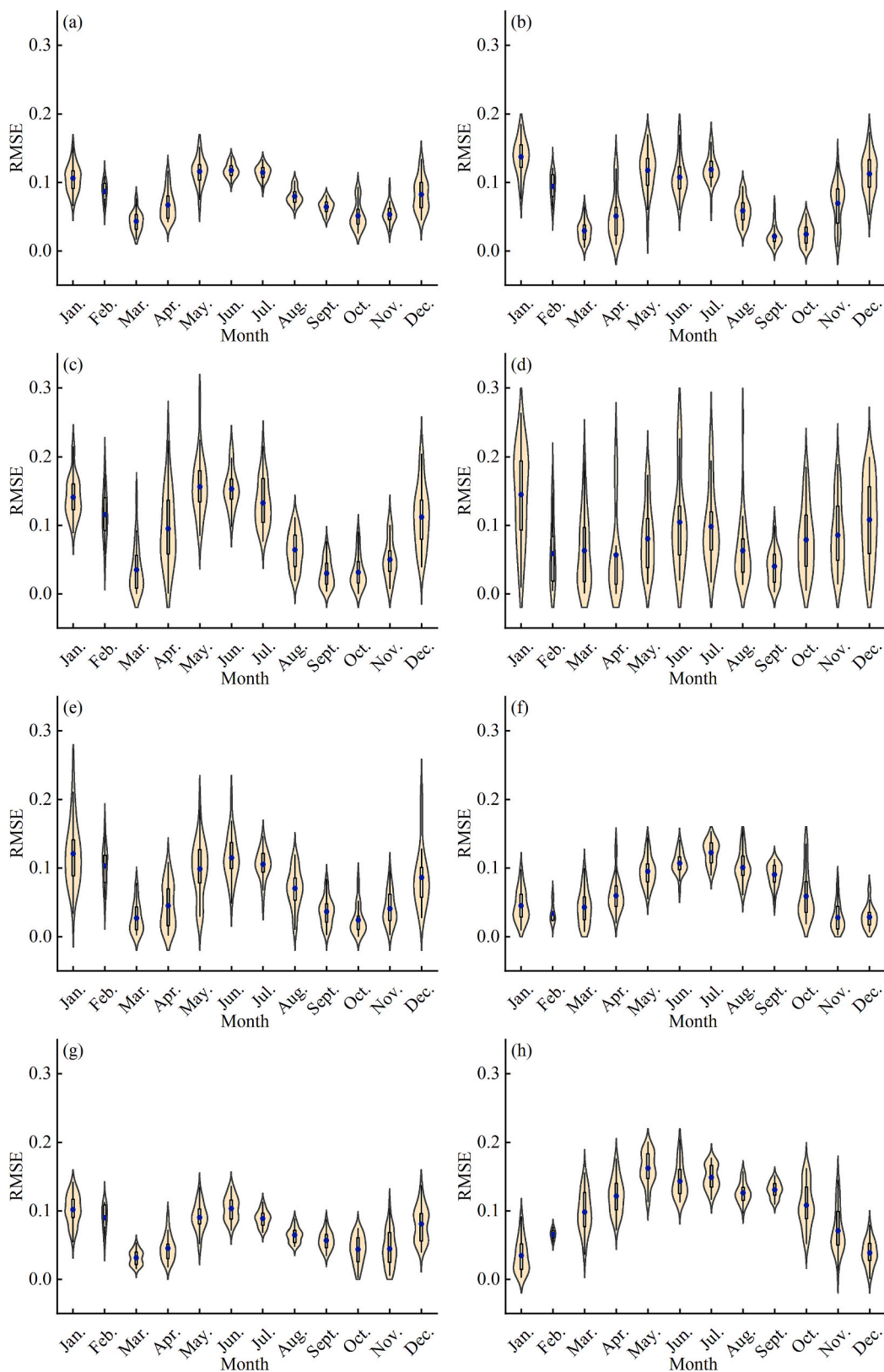
Fig. 6. Violin plots of RMSE by month: (a) China, (b) region I, (c) region II, (d) region III, (e) region IV, (f) region V, (g) region VI, (h) region VII.
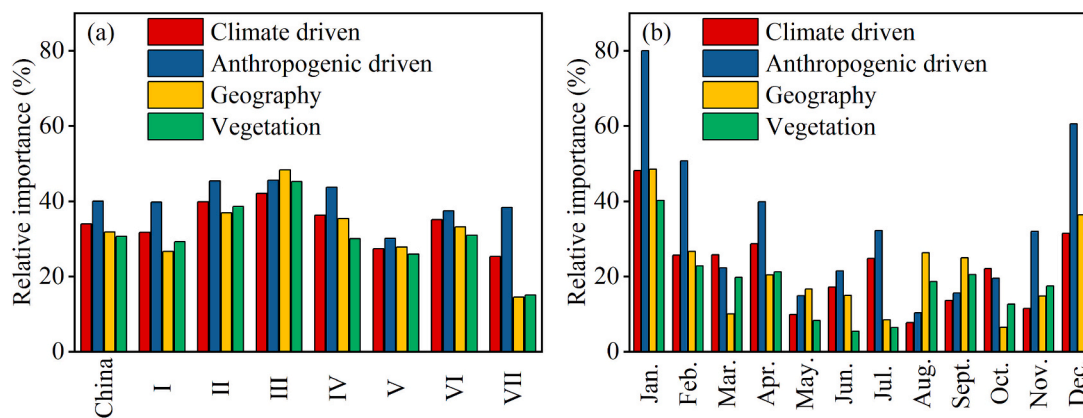
Fig. 7. Relative importance of input features for specific (a) region, (b) month.

LST most notably in August and September.

5. Discussion

5.1. Selection of input factors and time-continuous LST simulation accuracy

LST is an essential geophysical parameter closely associated with the energy and water balance of the land-atmosphere system (Ermida et al., 2017; Zhang et al., 2021). Based on the radiative transfer equation, the Sun, as the primary energy provider, interacts with the atmosphere (exchange layer) by transferring energy. Absorption of this energy is influenced by the attributes of the Earth's surface (Li et al., 2013). The LR and SR play critical roles in determining the total amount of energy in the atmosphere (Wild, 2015). CC, RH, and aerosols (NL) also affect energy exchange in the atmosphere (Stephens and Webster, 1981; Compo and Sardeshmukh, 2009; Pfeifroth et al., 2018). Moreover, Em and Al influence surface energy absorption, whereas LHF, SHF, and Wv/ Wu are key factors in determining the magnitude of energy loss (Li et al., 2013; Kafy et al., 2020). The influence of geography (Dem, slope, and aspect) on incoming solar radiation varies according to elevation and orientation factors (Phan et al., 2018). Vegetation (NDVI) can not only directly block the solar radiation reaching the surface but also humidify and cool the surrounding environment through evapotranspiration (Peñuelas et al., 2009; Abera et al., 2020). Land-use type (CLCD) can objectively characterize the level of utilization, transformation, and development of the Earth's surface through human activity. This serves as the most visually identifiable representation of how human activities affect the exchange of energy on land surfaces (Zhu et al., 2022a, 2022b). The aforementioned factors have a direct or indirect impact on energy exchange, which consequently influences variations in LST. Even when opting for the DL model, it is crucial to comprehensively consider the underlying physical mechanisms of the factors influencing LST (Zhao and Duan, 2020).

With the development of "Earth big data," the expeditious progression of machine learning techniques has created unprecedented opportunities for the development of innovative approaches to environmental monitoring (Yuan et al., 2020). Furthermore, DL models have demonstrated superior performance compared to conventional models, leading to significant advancements in the field of Earth environmental monitoring using remote sensing data (LeCun et al., 2015). The details of the spatial distribution (0.1°) of LST on a randomly selected day are shown in Fig. S2. The model was established based on the labels of high-density LST observation stations and was utilized to invert high-accuracy LST measurements across China. This study incorporated deep supervision and multiscale jump investigation into the selected U-Net++ model to enhance its completeness. This modification addresses the issue of unattainable back propagation and enables the acquisition and integration

of features from different levels through feature superposition. Consequently, the accuracy of the simulation was significantly enhanced, ensuring greater reliability.

The "big data" has become the solid foundation of environmental monitoring. Notably, when utilizing high-density station data, our findings indicated that the density of a particular station does not have a significant impact on the accuracy of the simulation. This demonstrates that China's meteorological observation stations fundamentally fulfilled the observation requirements. Although the station density was lower in the Qinghai-Tibet Plateau region than in other regions, the accuracy of LST inversion was not affected, which may also be related to the uniformity of the underlying surface. Compared with other relevant studies, the precision of air temperature retrieval is negatively impacted by a reduction in station density because the study used only 829 meteorological stations spread across mainland China (Shen et al., 2020).

5.2. Contribution of each input factor to LST

LST is determined by anthropogenic activities, geography, and surface and atmospheric interactions. Surface conditions due to anthropogenic activities, such as vegetation type, coverage, and soil moisture, affect LST by controlling the exchange of energy and water with the atmosphere (Jin and Dickinson, 2010). Alterations in the incoming solar radiation and atmospheric longwave radiation have a direct impact on LST trends by affecting the energy supply (Wang et al., 2014). As the primary energy input to Earth's climate system, incoming solar radiation serves as the prime determinant of the planet's energy budget (Wild, 2015). Fluctuations in incoming solar radiation directly affect the LST trend by modifying the energy provision at the Earth's surface. Incoming longwave radiation impacts LST by heating the Earth's surface (Pfeifroth et al., 2018; Abera et al., 2020). The majority of the longwave radiation emitted from the surface is absorbed by the atmosphere, and a significant portion is subsequently re-emitted to raise the temperature of the Earth's surface. Despite the significant influence of climatic drivers on LST, the present investigation revealed that the most noteworthy impact of anthropogenic drivers on LST occurred in China. The surface plays a significant role in climate formation and influences the exchange of surface heat, momentum, water vapor, and interaction processes involving the Earth's gases (Krishnan et al., 2020; Ren et al., 2021). For instance, artificially impermeable surfaces exhibit elevated heat retention properties owing to their rapid heat absorption rate, limited specific heat capacity, and radiation interception effects on urban structures. Incessant thermal emissions resulting from human activities and livelihoods, along with augmented greenhouse gas discharge, fortify atmospheric insulation and temperature inversion effects (Yang and Huang, 2021). All these phenomena exert a direct, indirect, and continuous influence on the heat balance and spatial distribution of the urban area and its vicinity, consequently impacting LST. As reported by the IPCC

AR6, there is strong evidence to suggest that human activities exert a substantial influence on the climate system across various dimensions (IPCC, 2021). Vegetation is a crucial indicator of local ecological sensitivity and vulnerability and exerts an irreplaceable influence on LST alteration. Vegetation effectively diminishes the amount of solar radiation transmitted to the ground through the reflection and absorption of a portion of the solar radiation (Ren et al., 2021). Generally, the interplay between natural and anthropogenic variables engenders intricate and indeterminate changes in LST, warranting continued and exhaustive long-term surveillance and investigation.

5.3. Limitations and developments

Compared to PMW remote sensing, TIR remote sensing is the optimal approach for acquiring LST data, exhibiting superior inversion accuracy. However, LST applications of TIR in various fields are severely limited by their inability to penetrate clouds. A previous study indicated that the average cloud cover on a global scale has the potential to exceed 70 %, leading to a potential reduction in the mean annual LST by 0.2–2 K (Mercury et al., 2012). Several methods have been developed to reconstruct time-continuous LST (Xu and Cheng, 2021; Mo et al., 2021; Zhang et al., 2021; Zhu et al., 2022a, 2022b): (1) spatial and temporal interpolation methods, (2) statistical regression methods, (3) surface energy balance methods, (4) PMW-based LST methods, and (5) machine learning. Currently, there are various all-weather reliable LST products with high spatiotemporal resolution in China, including: TRIMS (Thermal and Reanalysis Integrating Moderate-resolution Spatial-seamless, CSTR: 18406.11.Meteoro.tpdc.271252), ELITE (Essential thermaL Infrared remoTe sEnsing, CSTR: 18406.11.Meteoro.tpdc.271657) LST product datasets (Zhou et al., 2017; Zhang et al., 2019; Quan and Cheng, 2020; Quan et al., 2020; Xu and Cheng, 2021; Zhang et al., 2021). Although advancements have been made in the reconstruction of LST for cloud-covered pixels, the techniques presently suggested continue to be constrained in microwave monitoring by suboptimal precision and limited practicality. In this study, within the framework of "Earth big data", high-density station data and microwave data were utilized to enhance the capability of microwave monitoring of LST to the greatest extent possible. The amalgamation of TIR and PMW-merged LST is considered the optimal solution for creating an all-weather LST product at the present technical level. This approach is favored because of the complementary properties of TIR- and PMW-based LST (Xu and Cheng, 2021). Nevertheless, it is necessary to continue researching and developing methods to overcome surface penetration depth disparities between TIR- and PMW-based LST data while also improving the accuracy and resolution of PMW-based LST estimates (Li et al., 2023). Geostationary satellites should be strengthened in LST reconstruction, such as Himawari-8, FengYun-4 A, and Geostationary Operational Environmental Satellite R-Series, which improve temporal resolution compared with conventional sensors (Yamamoto et al., 2023).

The temporal simulation analysis results demonstrated a discernible and dynamic pattern fluctuating in a W-shape in China. Temporal LST simulations should be considered in future studies using DL models, such as the long short-term memory (LSTM) model. Notably, the structure of the DL model is intricate and encompasses numerous parameters, necessitating reliance on operational expertise and multiple iterations during the debugging phase, which consequently contribute to a certain reduction in the overall work efficiency (Wu et al., 2022). When the Adam algorithm with a rapid rate of convergence to improve computing efficiency was utilized as the optimizer in the present study, the loss function value of the model experienced the most precipitous decline in the training set, ultimately stabilizing at a satisfactory level (Zhou et al., 2018; Zheng et al., 2022).

The field of LST remote sensing monitoring has developed a plethora of refined physical models that are deeply rooted in systematic physical theories (Yuan et al., 2020). Currently, the potential of DL to supersede physical models is debated. DL has frequently been employed as a complementary tool to conventional physical models because of its ability to accurately mimic physical processes and streamline the calculations required for LST remote sensing. In future LST simulations, integrating a physical model with DL may enhance the accuracy of simulations (Mao et al., 2007; Mao et al., 2008). Uncertainties frequently manifest in the physical parameters, leading to inaccuracies in their outputs. By incorporating actual observations and supplementary data, the implementation of DL techniques has the potential for model output calibration. For instance, the accuracy of maximum air temperature simulations can be improved by incorporating Global Land Data assimilation system simulations (e.g., SM content and albedo) into the DL architecture (Di et al., 2016; Shen et al., 2020). To adhere to the principles of physical laws and mechanisms, DL architectures must be formulated for LST remote sensing, which entails a profound fusion of physics and DL (Schütt et al., 2017). Furthermore, physical regularization constraints are incorporated into the loss function of the DL models, leveraging insights from physical mechanisms and knowledge to ensure that LST modeling maintains physical consistency. The loss function, which is limited by physical constraints, is subsequently optimized to achieve a satisfactory outcome that exhibits superior model performance and adherence to physical consistency (Yuan et al., 2020). Overall, the combination of physical simulation and DL can not only improve the accuracy of LST but also improve the physical interpretability in LST remote sensing monitoring.

5.4. Implications for management

The findings of this study have significant implications for management and can be summarized into three key points. First, the present density of meteorological stations is sufficient for remote-sensing monitoring, thereby achieving the desired accuracy. Second, although microwave remote sensing has the advantage of being able to continuously monitor surface information through clouds for extended periods, its spatial resolution is significantly inferior to that of TIR remote sensing. There is thus a need to reinforce the establishment of microwave remote sensing technology to enhance its spatial resolution capabilities. Finally, LST plays a crucial role as a variable in the process of water heat exchange and energy balance and should be strengthened for use in relevant studies. For example, time-continuous LST can accurately depict the state of surplus and deficiency of soil moisture. It operates based on the principle that the heat capacity of water is higher than that of other media. Furthermore, this technique posits that the greater the temperature variance between day and night, the more pronounced the water shortage and drought, which in turn allows for the direct assessment of actual drought and flood conditions. However, studies on these topics are scarce.

6. Conclusion

In this study, the U-Net family DL model was employed to estimate LST for the first time. Microwave remote sensing data derived from the FY-3C/3D satellites and high-density station observations (>10,000 stations) were input into the DL model. According to radiation transmission, climate, anthropogenic, geographical, and vegetation datasets were considered to facilitate a multi-source data fusion approach for LST estimation. Compared with the U-Net and U^2-Net models, the U-Net++ model with modified skip connections considered the non-linear relationship more effectively, leading to an improved overall model performance. The precision of the LST simulation demonstrated advantageous results in both spatial and temporal domains, as evidenced by the validation data. Through the utilization of high-density stations, our research indicated that station density does not significantly affect inversion precision. In addition, the average RMSE change in China fluctuated in a W-shape, indicating that the simulation accuracy exhibited very strong monthly changes. Finally, the results showed that anthropogenic driving was the dominant factor affecting LST in

China, with an RI of 40.05 %. This is because the CLCD caused by human activities has a direct impact on the transformation. The RIs of climate-driven, geographical, and vegetation factors were 33.98 %, 31.87 %, and 30.72 %, respectively.

It should be noted that there were several limitations to our investigation which future research studies should seek to improve. First, the combination of LST data obtained from thermal TIR and PMW measurements is widely recognized as the most viable approach for creating an all-weather LST product using existing technology. Second, the LST simulation accuracy in our study changed over time, and temporal LST simulations should be considered in future studies with DL models, such as the LSTM model. Finally, our model did not simulate LST accurately under extreme temperature conditions because the DL model is not constrained by physical conditions. It is highly recommended that future studies should integrate physical models and DL for environmental remote-sensing applications. This integration can be applied through various methods, including DL calibration using physical model outputs, DL architecture design guided by physical principles, and DL modeling constrained by physical assumptions. In conclusion, although the utilization of efficient multi-source datasets can enhance the precision of models, the scientific elimination of variables that are susceptible to causing uncertainties in remote sensing monitoring accuracy remains a major challenge.

CRediT authorship contribution statement

Jiahao Han: Writing – original draft, Visualization, Data curation, Conceptualization. **Shibo Fang:** Writing – review & editing, Supervision, Funding acquisition, Conceptualization. **Qianchuan Mi:** Formal analysis. **Xinyu Wang:** Methodology. **Yanru Yu:** Software. **Wen Zhuo:** Validation. **Xiaofeng Peng:** Investigation.

Declaration of competing interest

The authors declare that they have no known competing financial interests or personal relationships that could have appeared to influence the work reported in this paper.

Data availability

The authors do not have permission to share data.

Acknowledgements

Appendix A. Supplementary data

Supplementary data to this article can be found online at https://doi.org/10.1016/j.scitotenv.2024.169992.

References

Abera, T., Heiskanen, J., Maeda, E., Pellikka, P., 2020. Land Surface Temperature Trend and its Drivers in East Africa. J. Geophys. Res, Atmos, p. 125.

Anderson, M., Hain, C., Wardlow, B., Pimstein, A., Mecikalski, J., Kustas, W., 2011. Evaluation of drought indices based on thermal remote sensing of evapotranspiration over the continental United States. J. Clim. 24 (8), 2025–2044.

Arigbe, O., Oyeneyin, B., Arana, I., Droubi, M., 2018. Real-Time Relative Permeability Prediction Using Deep Learning. J. Pet. Explor. Prod, Technol, p. 9.

Azarderakhsh, M., Prakash, S., Zhao, Y., AghaKouchak, A., 2020. Satellite-based analysis of extreme land surface temperatures and diurnal variability across the hottest place on earth. IEEE Geosci. Remote Sens. Lett. 17, 2025–2029.

Benali, A., Carvalho, A.C., Nunes, J.P., Carvalhais, N., Santos, A., 2012. Estimating air surface temperature in Portugal using MODIS LST data. Remote Sens. Environ. 124, 108–121.

Chen, T.H.K., Pandey, B., Seto, K.C., 2023. Detecting subpixel human settlements in mountains using deep learning: a case of the Hindu Kush Himalaya 1990–2020. Remote Sens. Environ. 294, 113625.

Chen, X., Gao, F., Li, Y., Wang, B., Li, X., 2022. All-weather and superpixel water extraction methods based on multisource remote sensing data fusion. Remote Sens. 14, 6177.

Coll, C., Valor, E., Galve, J., Mira, M., Bisquert, M., Garcia-Santos, V., Caselles, E., Caselles, V., 2012. Long-term accuracy assessment of land surface temperatures derived from the advanced along-track scanning radiometer. Remote Sens. Environ. 116, 211–225.

Compo, G., Sardeshmukh, P., 2009. Oceanic influences on recent continental warming. Clim. Dyn. 32, 333–342.

Dalagnol, R., Wagner, F.H., Galvão, L.S., Braga, D., Osborn, F., Sagang, L.B., Bispo, P.D. C., Payne, M., Silva Junior, C., Favrichon, S., Silgueiro, V., Anderson, L.O., Aragão, L. E.O.C., Fensholt, R., Brandt, M., Ciais, P., Saatchi, S., 2023. Mapping tropical forest degradation with deep learning and planet NICFI data. Remote Sens. Environ. 298, 113798.

Davis, P., Nicholls, K., Holland, D., Schmidt, B., Washam, P., Riverman, K., Arthern, R., Vaňková, I., Eayrs, C., Smith, J., Anker, P., Mullen, A., Dichek, D., Lawrence, J., Meister, M., Clyne, E., Basinski-Ferris, A., Rignot, E., Queste, B., Makinson, K., 2023. Suppressed basal melting in the eastern Thwaites glacier grounding zone. Nature 614, 479–485.

Di, Q., Schwartz, J., Koutrakis, P., 2016. A hybrid prediction model for PM2.5 mass and components using a chemical transport model and land use regression. Atmos. Environ. 131.

Donohoe, A., Armour, K.C., Pendergrass, A.G., Battisti, D.S., 2014. Shortwave and longwave radiative contributions to global warming under increasing CO_2. Proc. Natl. Acad. Sci. 111 (47), 16700–16705.

Ermida, S., Dacamara, C., Trigo, I., Pires, A., Ghent, D., Remedios, J., 2017. Modelling directional effects on remotely sensed land surface temperature. Remote Sens. Environ. 190, 56–69.

Ghahremanloo, M., Mobasheri, M., Amani, M., 2018. Soil moisture estimation using land surface temperature and soil temperature at 5 cm depth. Int. J. Remote Sens. 40, 1–14.

Göttsche, F.M., Olesen, F., Trigo, I., Bork-Unkelbach, A., Martin, M., 2016. Long term validation of land surface temperature retrieved from MSG/SEVIRI with continuous in-situ measurements in Africa. Remote Sens. 8, 410.

Hollmann, R., Merchant, C., Saunders, R., Downy, C., Buchwitz, M., Cazenave, Chuvieco, E., Defourny, P., De Leeuw, G., Forsberg, R., Holzer-Popp, T., Paul, F., Sandven, S., Sathyendranath, S., Van Roozendael, M., Wagner, W., 2013. The ESA climate change initiative: satellite data records for essential climate variables. Bull. Am. Meteorol. Soc. 94, 1541–1552.

IPCC, 2021. Climate Change 2021: The Physical Science Basis. Cambridge University Press, New York.

Jeong, S., Ko, J., Yeom, J.-M., 2021. Predicting rice yield at pixel scale through synthetic use of crop and deep learning models with satellite data in South and North Korea. Sci. Total Environ. 802, 149726.

Jin, M., Dickinson, R., 2010. Land surface skin temperature climatology: benefitting from the strengths of satellite observations. Environ. Res. Lett. 5, 044004.

Kafy, A.A., Faisal, A.A., Sikdar, S., Hasan, M., Rahman, M., Khan, M.H., Islam, R., 2020. Impact of LULC changes on LST in Rajshahi District of Bangladesh: a remote sensing approach. Aust. Geogr. Stud. 3, 11–23.

Karimi Firozjaei, M., Kiavarz, M., Alavi Panah, S.K., 2022. Satellite-derived land surface temperature spatial sharpening: a comprehensive review on current status and perspectives. Eur. J. Remote Sens. 55, 644–664.

Kohn, J., Royer, A., 2010. AMSR-E Data Inversion for Soil Temperature Estimation under Snow Cover. Remote Sens, Environ, p. 114.

Krishnan, P., Meyers, T., Hook, S., Heuer, M., Senn, D., Dumas, E., 2020. Intercomparison of situ sensors for ground-based land surface temperature measurements. Sensors 20.

LeCun, Y., Bengio, Y., Hinton, G., 2015. Deep learning. Nature 521 (7553), 436–444.

Lee, C.S., Sohn, E., Park, J., Jang, J.-D., 2018. Estimation of soil moisture using deep learning based on satellite data: a case study of South Korea. GIsci. Remote Sens. 56, 1–25.

Li, Z., Tang, B., Wu, H., Yan, G., Wan, Z., Trigo, I., Sobrino, J., 2013. Satellite-derived land surface temperature: current status and perspectives. Remote Sens. Environ. 131, 14–37.

Li, Z., Wu, H., Duan, S., Zhao, W., Liu, X., Leng, P., Tang, R., Ye, X., Zhu, J., Sun, Y., Si, M., Liu, M., Li, J., Zhang, X., Shang, G., Tang, B., Yan, G., Zhou, C., 2023. Satellite Remote Sensing of Global Land Surface Temperature: Definition, Methods, Products, and Applications. Rev, Geophys, p. 61.

Liu, S., Zhao, X., Zhang, F., Qiu, A., Chen, L., Huang, J., Chen, S., Zhang, S., 2022. Spatial downscaling of NPP-VIIRS nighttime light data using multiscale geographically weighted regression and multi-source variables. Remote Sens. 14, 6400.

Lobert, F., Löw, J., Schwieder, M., Gocht, A., Schlund, M., Hostert, P., Erasmi, S., 2023. A deep learning approach for deriving winter wheat phenology from optical and SAR time series at field level. Remote Sens. Environ. 298, 113800.

Malakar, N., Hulley, G., 2016. A water vapor scaling model for improved land surface temperature and emissivity separation of MODIS thermal infrared data. Remote Sens. Environ. 182, 252–264.

Mao, K., Shi, J., Li, Z., Tang, H., 2007. An RM-NN algorithm for retrieving land surface temperature and emissivity from EOS/MODIS data. J. Geophys. Res. Atmos. 112, 1.

Mao, K., Shi, J., Tang, H., Li, Z., Wang, X., Chen, K., 2008. A neural network technique for separating land surface emissivity and temperature from ASTER imagery. IEEE Trans. Geosci. Remote Sens. 46, 200–208.

Mao, K., Zhiyuan, Z., Shen, X., Xu, T., Chunyu, G., Guang, L., 2018. Retrieval of land-surface temperature from AMSR2 data using a deep dynamic learning neural network. Chin. Geogr. Sci. 28 (1), 1–11.

Marchand, N., Royer, A., Krinner, G., Roy, A., Langlois, A., Vargel, C., 2018. Snow-covered soil temperature retrieval in Canadian Arctic permafrost areas, using a land surface scheme informed with satellite remote sensing data. Remote Sens. 10, 1703.

Mercury, M., Green, R., Hook, S., Oaida, B., Wu, W., Gunderson, A., Chodas, M., 2012. Global cloud cover for assessment of optical satellite observation opportunities: a HyspIRI case study. Remote Sens. Environ. 126, 62–71.

Mo, Y., Xu, Y., Chen, H., Zhu, S., 2021. A review of reconstructing remotely sensed land surface temperature under cloudy conditions. Remote Sens. 13, 2838.

Nogueira, M., Hurduc, A., Ermida, S., Lima, D., Soares, P.M.M., Johannsen, F., Dutra, E., 2022. Assessment of the Paris urban heat island in ERA5 and offline SURFEX-TEB (v8.1) simulations using the METEOSAT land surface temperature product. Geosci. Model Dev. 15, 5949–5965.

Osińska-Skotak, K., 2007. Studies of soil temperature on the basis of satellite data. Int. Agrophys. 21, 275–284.

Ouzounov, D., Freund, F., 2004. Mid-infrared emission prior to strong earthquakes analyzed by remote sensing data. Adv. Space Res. 33, 268–273.

Penghai, W., Yin, Z., Yang, H., Wu, Y., Ma, X., 2019. Reconstructing geostationary satellite land surface temperature imagery based on a multiscale feature connected convolutional neural network. Remote Sens. 11, 300.

Peñuelas, J., Rutishauser, T., Filella, I., 2009. Phenology feedbacks on climate change. Science 324 (5929), 887–888.

Pfeifroth, U., Sanchez-Lorenzo, A., Manara, V., Trentmann, J., Hollmann, R., 2018. Trends and variability of surface solar radiation in Europe based on surface and satellite based data records. J. Geophys. Res. Atmos. 123, 1735–1754.

Phan, T.N., Kappas, M., Tran, T., 2018. Land surface temperature variation due to changes in elevation in Northwest Vietnam. Climate 6, 28.

Qin, X., Zhang, Z., Huang, C., Dehghan, M., Zaïane, O., Jagersand, M., 2020. U2-net: going deeper with nested U-structure for salient object detection. Pattern Recogn. 106, 107404.

Quan, Z., Cheng, J., 2020. An empirical algorithm for retrieving land surface temperature from AMSR-E data considering the comprehensive effects of environmental variables. Earth Space Sci. 7 e2019EA001006.

Quan, Z., Wang, N., Cheng, J., Xu, S., 2020. A stepwise downscaling method for generating high-resolution land surface temperature from AMSR-E data. IEEE J. Sel. Top. Appl. Earth Obs. Remote Sens. 13, 5669–5681.

Reichstein, M., Camps-Valls, G., Stevens, B., Jung, M., Denzler, J., Carvalhais, N., Prabhat, M., 2019. Deep learning and process understanding for data-driven earth system science. Nature 566, 195.

Ren, T., Zhou, W., Wang, J., 2021. Beyond intensity of urban heat island effect: a continental scale analysis on land surface temperature in major Chinese cities. Sci. Total Environ. 791, 148334.

Ronneberger, O., Brox, F.a.T., 2015. U-Net: Convolution Networks for Biomedical Image Segmentation. (In, arXiv e-prints).

Royer, A., Poirier, S., 2010. Surface temperature spatial and temporal variations in North America from homogenized satellite SMMR-SSM/I microwave measurements and reanalysis for 1979-2008. J. Geophys. Res. 115, D08110.

Schütt, K., Arbabzadah, F., Chmiela, S., Müller, K.R., Tkatchenko, A., 2017. Quantum-chemical insights from deep tensor neural networks. Nat, Commun. p. 8.

Shen, H., Jiang, Y., Li, T., Cheng, Q., Zeng, C., Zhang, L., 2020. Deep learning-based air temperature mapping by fusing remote sensing, station, simulation and socioeconomic data. Remote Sens. Environ. 240, 111692.

Song, X., Ganlin, Z., Liu, F., Li, D., Zhao, Y., Yang, J., 2016. Modeling spatio-temporal distribution of soil moisture by deep learning-based cellular automata model. J. Arid. Land 8, 734–748.

Stephens, G.L., Webster, P.J., 1981. Clouds and climate: sensitivity of simple systems. J. Atmos. Sci. 38 (2), 235–247.

Tan, J., Esmaeel, N., Mao, K., Shi, J., Li, Z.-L., Xu, T., Yuan, Z., 2019. Deep learning convolutional neural network for the retrieval of land surface temperature from AMSR2 data in China. Sensors 19, 2987.

Thakur, G., Schymanski, S., Mallick, K., Trebs, I., Sulis, M., 2022. Downwelling longwave radiation and sensible heat flux observations are critical for surface temperature and emissivity estimation from flux tower data. Sci. Res. 12.

Townsend, J., Justice, C., Skole, D., Malingreau, J.P., Cihlar, J., Ms, T., Sadowski, F., Ruttenberg, S., 1994. The 1 km resolution global data set: needs of the international geosphere biosphere Programme. Int. J. Remote Sens. 15, 3417–3441.

Wan, Z.M., Li, Z., 1997. A physics-based algorithm for retrieving land-surface emissivity and temperature form Eos/MODIS data. IEEE Trans. Geosci. Remote Sens. 34, 892–905.

Wang, A., Barlage, M., Zeng, X., Draper, C., 2014. Comparison of land skin temperature from a land model, remote sensing, and in situ measurement: comparison of land skin temperature. J. Geophys. Res. 119 (6), 3093–3106.

Wang, G., Ma, X., Hagan, D., van der Schalie, R., Kattel, G., Ullah, W., Tao, L., Lijuan, M., Liu, Y., 2022. Towards consistent soil moisture records from China's FengYun-3 microwave observations. Remote Sens. 14, 1225.

Wang, N., Li, Z., Tang, B., Zeng, F., Li, C., 2013. Retrieval of atmospheric and land surface parameters from satellite-based thermal infrared hyperspectral data using a neural network technique. Int. J. Remote Sens. 34, 3485–3502.

Wang, Z., Yang, P., Liang, H., Zheng, C., Yin, J., Tian, Y., Cui, W., 2021. Semantic segmentation and analysis on sensitive parameters of Forest fire smoke using smoke-Unet and Landsat-8 imagery. Remote Sens. 14, 45.

Westerling, A., Hidalgo, H., Cayan, D.R., Swetnam, T., 2006. Warming and earlier spring increase western US forest wildfire activity. Science 1161, 1–9.

Wild, M., 2015. Decadal changes in radiative fluxes at land and ocean surfaces and their relevance for global warming. Wiley Interdiscip rev. Clim. Chang. 7.

Wolanin, A., Mateo-García, G., Camps-Valls, G., Gómez-Chova, L., Meroni, M., Duveiller, G., You, L., Guanter, L., 2020. Estimating and understanding crop yields with explainable deep learning in the Indian Wheat Belt. Environ. Res, Lett, p. 15.

Wu, F., Wang, C., Zhang, H., Li, J., Li, L., Chen, W., Zhang, B., 2021. Built-up area mapping in China from GF-3 SAR imagery based on the framework of deep learning. Remote Sens. Environ. 262, 112515.

Wu, J., Hu, C., Liu, R., Wu, S., Cao, J., Cheng, Z., Yu, B., Lei, Z., 2022. Adam SPGD algorithm in freeform surface in-process interferometry. Opt. Express 30.

Xu, S., Cheng, J., 2021. A new land surface temperature fusion strategy based on cumulative distribution function matching and multiresolution Kalman filtering. Remote Sens. Environ. 254, 112256.

Yamamoto, Y., Ichii, K., Ryu, Y., Kang, M., Murayama, S., Kim, S.-J., Cleverly, J., 2023. Detection of vegetation drying signals using diurnal variation of land surface temperature: application to the 2018 East Asia heatwave. Remote Sens. Environ. 291, 113572.

Yang, J., Huang, X., 2021. The 30 m annual land cover dataset and its dynamics in China from 1990 to 2019. Earth Syst. Sci. Data 13, 3907–3925.

Yao, N., Li, Y., Lei, T., Peng, L., 2018. Drought evolution, severity and trends in mainland China over 1961-2013. Sci. Total Environ. 616-617, 73–89.

Yuan, Q., Shen, H., Li, T., Li, Z., Li, S., Jiang, Y., Xu, H., Tan, W., Yang, Q., Wang, J., Gao, J., Zhang, L., 2020. Deep learning in environmental remote sensing: achievements and challenges. Remote Sens. Environ. 241, 111716.

Zhang, L., Zhang, L., Du, B., 2016. Deep learning for remote sensing data: a technical tutorial on the state of the art. IEEE Geosci. Remote Sens. Mag. 4, 22–40.

Zhang, X., Zhou, J., Göttsche, F.-M., Zhan, W., Shaomin, L., Cao, R., 2019. A method based on temporal component decomposition for estimating 1-km all-weather land surface temperature by merging satellite thermal infrared and passive microwave observations. IEEE Trans. Geosci. Remote Sens. PP 1–22.

Zhang, X., Zhou, J., Liang, S., Wang, D., 2021. A practical reanalysis data and thermal infrared remote sensing data merging (RTM) method for reconstruction of a 1-km all-weather land surface temperature. Remote Sens. Environ. 260, 112437.

Zhao, W., Duan, S.B., 2020. Reconstruction of daytime land surface temperatures under cloud-covered conditions using integrated MODIS/Terra land products and MSG geostationary satellite data. Remote Sens. Environ. 247, 111931.

Zheng, Y., Wang, R., Chen, C., Meng, F., 2022. Fast stability assessment of rock slopes subjected to flexural toppling failure using adaptive moment estimation (Adam) algorithm. Landslides 19.

Zhou, J., Zhang, X., Zhan, W., Göttsche, F.M., Shaomin, L., Olesen, F., Hu, W., Dai, F., 2017. A thermal sampling depth correction method for land surface temperature estimation from satellite passive microwave observation over barren land. IEEE Trans. Geosci. Remote Sens. PP 1–14.

Zhou, Y., Zhang, Y., Wang, R., Chen, H., Zhao, Q., Liu, B., Shao, Q., Cao, L., Sun, S., 2023. Deep learning for daily spatiotemporally continuity of satellite surface soil moisture over eastern China in summer. J. Hydrol. 619, 129308.

Zhou, Z., Rahman Siddiquee, M.M., Tajbakhsh, N., Liang, J., 2018. UNet++: A nested U-Net architecture for medical image segmentation. (In, arXiv e-prints).

Zhu, X., Duan, S.B., Li, Z.L., Penghai, W., Wu, H., Zhao, W., Qian, Y., 2022a. Reconstruction of land surface temperature under cloudy conditions from Landsat 8 data using annual temperature cycle model. Remote Sens. Environ. 281, 113261.

Zhu, Z., Qiu, S., Ye, S., 2022b. Remote sensing of land change: a multifaceted perspective. Remote Sens. Environ. 282, 113266.